



X-ray imaging of tumor growth in live mice by detecting gold-nanoparticle-loaded cells

Chia-Chi Chien^{1,2}, Hsiang-Hsin Chen¹, Sheng-Feng Lai¹, Y. Hwu^{1,2,3}, Cyril Petibois⁴, C. S. Yang⁵, Y. Chu⁶ & G. Margaritondo⁷

SUBJECT AREAS:

NANOBIOTECHNOLOGY

NANOPARTICLES

NANOPHOTONICS

IMAGING

Received
9 March 2012

Accepted
10 May 2012

Published
29 August 2012

Correspondence and requests for materials should be addressed to Y.H. (phhwu@sinica.edu.tw)

¹Institute of Physics, Academia Sinica, Nankang, Taipei 115, Taiwan, ²Department of Engineering and System Science, National Tsing Hua University, Hsinchu 300, Taiwan, ³Advanced Optoelectronic Technology Center, National Cheng Kung University, Tainan 701, Taiwan, ⁴Université de Bordeaux, CNRS UMR 5248 - CBMN, F33405 Talence-Cedex, France, ⁵Center for Nanomedicine Research, National Health Research Institutes, Miaoli 350, Taiwan, ⁶National Synchrotron Light Source II, Brookhaven National Laboratory, Upton 11973-5000, NY, USA, ⁷Ecole Polytechnique Fédérale de Lausanne (EPFL), CH-1015 Lausanne, Switzerland.

We show that sufficient concentrations of gold nanoparticles produced by an original synthesis method in EMT-6 and CT-26 cancer cells make it possible to detect the presence, necrosis and proliferation of such cells after inoculation in live mice. We first demonstrated that the nanoparticles do not interfere with the proliferation process. Then, we observed significant differences in the tumor evolution and the angiogenesis process after shallow and deep inoculation. A direct comparison with pathology optical images illustrates the effectiveness of this approach.

Gold nanoparticles (AuNPs) are already used as contrast agents^{1–5} in x-ray imaging. However, their applications to radiological cell tracing are still hindered by the limited upload in individual cells which gives insufficient image contrast. This is a serious handicap with respect to other techniques such as visible light⁶, X-ray⁷ fluorescence or Raman^{8,9} imaging. Such a limitation is regrettable since radiological cell tracing could otherwise provide very valuable information on physiological and pathological mechanisms. In particular, it could elucidate the mechanisms of cancer cell migration and their relations to tumor development. In this study, we present experimental evidence for the removal of the above limitation in cancer-cell-related tests in mice.

We succeeded in loading sufficient amounts of AuNPs, >50 pg/cell, in the cancer cells to effectively image them without affecting their functions and ability to proliferate. After inoculation in mice, we could detect the cells and accurately determine their positions thanks to the nanoparticle-induced contrast enhancement. This enabled us to monitor in detail the tumor growth. We could specifically analyze the relation between the primary (inoculated) cancer cells, their proliferation and the consequent tumor growth and metastasis.

The analysis was extended to the relation between cancer cell evolution and local tumor angiogenesis. For this, we imaged the tumor-related microvasculature by injecting a high-density BaSO₄ nanoparticle colloid as contrast agent and following its flow in the blood system. The monitoring was also performed in three dimensions (3D) by tomographic reconstruction, with ~1 μm resolution.

Finally, particularly interesting details were revealed by ultrahigh resolution x-ray imaging using a zone plate full-field transmission hard-x-ray microscope (TXM)^{10,11}. The instrumental resolution reached in this case ~20 nm.

Nanoparticles can find many possible applications in medicine¹² as drug carriers^{13–16}, biomarkers^{17–18}, biosensors¹⁹ and contrast agents^{1,20–22}. Surface modifications expand these applications by enabling them to target specific sites on cell surfaces^{23,24}, organelles, the nucleus or the extracellular matrix. Even without surface modification, AuNPs can be internalized in cells^{25–29}.

Previous publications reported that the type of cell line and the nanoparticle size influence the amount of uptaken AuNPs per cell²⁷. Our own research indicated that different cancer cell lines can internalize large amounts AuNPs without affecting viability^{30–32}.

Based on these facts, we selected for the present study bare AuNPs^{33–35} synthesized by intense x-ray irradiation as markers for EMT-6 and CT-26 cells to be inoculated in mice. The experiments were performed for tumors in



the thigh region, induced by shallow or deep inoculation, as well as for lung tumors induced by tail vein injection. After inoculation, the cancer cells were found not only at the injection site but also at nearby locations, revealing migration rather than just growth. Anomalous microvasculature was not confined to the injection site but primarily near the migrated cells.

We observed detectable differences in the tumor migration between shallow and deep injection of cancer cells. Specifically, there was less localized necrosis and more angiogenesis after deep injection. Finally, the tests on tail vein injection of cancer cells demonstrated the feasibility of revealing cancer development in faraway sites, specifically the lungs.

We also implemented this imaging strategy taking advantage of a new type of AuNP which emits photoluminescent red light when their core size is reduced to ~ 1 nm and capped by MUA (11-mercaptopundecanoic acid)³⁶. Similar to the bare AuNPs, large amount of coated AuNPs (MUA-AuNPs) can also be loaded to EMT-6 cells without affecting their viability and cell division. In addition to the X-ray, the fluorescence allows visible light imaging long time (>3 weeks) after the inoculation and after many generations of cell division. Preliminary test demonstrated that this approach can reveal the localization and the migration of cells, with a combined x-ray/visible imaging technique.

Results

The first part of the study concerned the uptake of sufficient quantities of AuNPs by the cells, and specifically their biocompatibility and their effects on cell proliferation. We used two types of AuNPs: bare AuNPs and MUA-AuNPs; both types we extensively tested^{33–36}. The one-pot, reducing agent free synthesis produced clean and monodisperse AuNPs with high colloidal stability. Optical microscopy and TEM tests on cell specimens in vitro confirmed that the AuNPs were internalized by endocytosis^{30–32} and did not penetrate into the cell nuclei. The nanoparticles were biocompatible with the cell lines we tested up to a concentration of 2.0 mM in the culture media. We also confirmed that 24 hours after exposure to the bare-AuNP colloid, a large number of AuNPs accumulated in the cytoplasm (Fig. 1a). After 7 days and as many as six cell cycles, the AuNPs were still present in $>20\%$ of the cells although the number per cell decreased (Fig. 1b). The optical image of Fig. 1c shows cells in the mitotic phase, indicating that AuNPs pass from the first cell generation to the next generations. The partition of the nanoparticles between daughter cells explains the decrease in the AuNP number per cell. We did not detect significant excretion of AuNPs during the cell culture period of 48 hours; however, we cannot rule out their possible excretion from cells via the lymphatic system or by other metabolic mechanisms after inoculation. The excretion would affect our quantitative assessments but not change the qualitative description of cell proliferation.

Quite interestingly, the growth rate of cells with AuNPs was similar to that of control cells not exposed to nanoparticles - see Fig. 1d - indicating good biocompatibility. Furthermore, Fig. 1e shows that the bare-AuNPs do not detectably influence the tumor growth. Even larger amounts of MUA-AuNPs were found internalized; however, we report here only on the bare AuNPs except otherwise mentioned.

The uploaded AuNPs made it possible to monitor the cancer growth and the simultaneous angiogenesis, as shown for example in Fig. 2, by microangiography. When the thigh tumor development reached day 3, angiogenesis had already initiated. In Fig. 2a, the darkest (high x-ray absorption) area is the inoculation site. Figure 2b corresponds to different times after the injection of contrast agent. One can readily see the progressive development of the microvasculature.

At day 7, the vessel density was higher than at day 3, as it can be seen in Figs. 2c–2e (taken in a similar region but on different mice with respect to Figs. 2a and b). Note that most AuNPs, and therefore

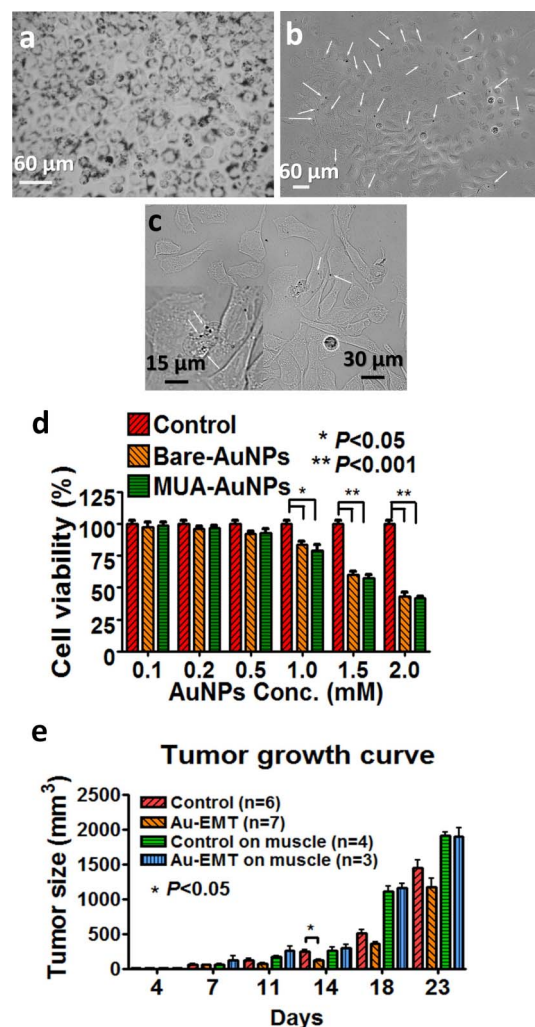


Figure 1 | (a) Optical images show 500 μM AuNPs internalized in all primary EMT-6 cells. (b) and (c): optical images at day 7 of culture of daughter EMT-6 cells produced by proliferation; note that the AuNP content per cell is reduced with respect to Fig. 1a; specifically, (c) shows EMT-6 cells, after 5 or 6 proliferation generations, still carried AuNPs in the mitotic phase. The arrows in Fig. 1b mark AuNP containing daughter cells. (d) Cell proliferation curve, i.e., the ratio between the cell numbers for AuNP-containing cells and control cells; this curve indicates that the AuNPs do not influence the proliferation process. (e) Tumor size for shallow (black and red) and deep (green and blue) inoculation, for AuNP and control cells (n: number of tested mice). The results showed no significant differences. Note the similarity of the results for AuNP-loaded cells and control cells. Only subcutaneous tumors showed differences at day 14. The ANOVA statistical analysis was performed by GraphPad Prism 4 software.

a large number of the mother tumor cells, remained inside the tumor region. Some tumor cells divided producing daughter cells. No angiogenesis was visible in the initial inoculation site. Figures 2d and 2e illustrate the same points with tomographically reconstructed 3D images. Figures 2f–2h show similar results for day 7 tumors induced by tumor cells without AuNPs.

Figure 3 reports data for day 9, clearly revealing the morphological characteristics of the microvasculature. In particular, substantial angiogenesis occurred around the inoculation site and the tumor core (Figs. 3e–3g). We also observed angiogenesis in regions where relatively few tumor cells were revealed by the uptaken AuNPs (Fig. 3c, tumor bottom, 3e and 3f).

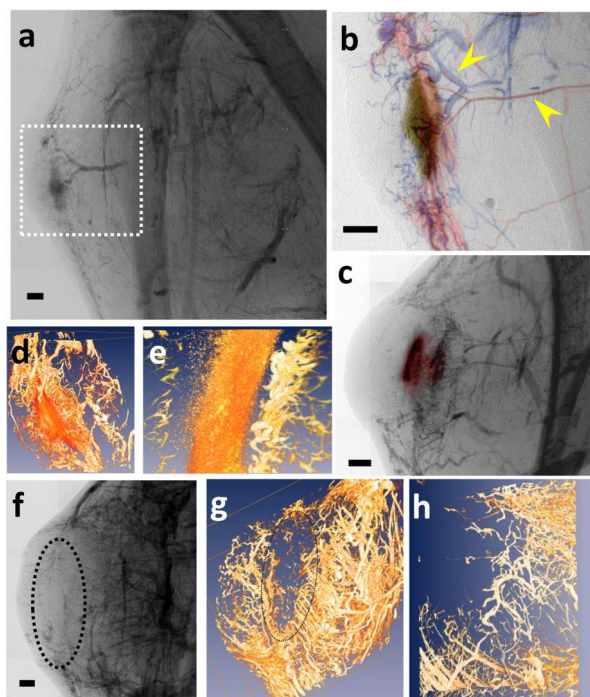


Figure 2 | (a) and (b): *in vivo* projection x-ray tumor images at day 3. (b): the magnified, color-coded view of the rectangular portion of (a), showing that the tumor already developed a vessel network with feeding arterioles (arrow, red color vessels) and venules (arrow head, blue color vessels). The brown area is the inoculated site. (c): projection image similar to (a), at day 7. (d) and (e): tomographic reconstructed images corresponding to (c) with two levels of magnification (supplementary data S2 d and e). Tumor angiogenesis at day 7 is denser than at day 3. Most of inoculated primary tumor cells stayed at the inoculation site and angiogenesis developed around but not inside the central area. (f)–(h): tomography results at day 7 without Au-NPs also show angiogenesis around but not inside the inoculation site (black dotted area). (f): projection image (the dotted circle marks the tumor whereas (g) and (h) are tomographic reconstructed image with low and high magnification (supplementary data S2 g and h). All scale bars are 500 μm .

The experiments revealed interesting differences in the tumor growth between deep and shallow inoculation in the thighs. Figure 4 shows results for deep inoculation sites. Overall, there is more proliferation than for shallow inoculation, resulting in less contrast in the tumor core, and more angiogenesis; these are indications of a more aggressive tumor development.

We still see in Fig. 4a regions with dead cells in the core (left arrow), but their density is much less than for shallow inoculation. On the contrary, a larger number of cells proliferated (right arrow). The proliferation decreased the AuNP content per cell because of the partition between daughter cells. This resulted in weaker image contrast.

We see in Fig. 4b and 4d that the proliferating cells are in deep locations around the inoculation site (but not confined to it as dead cells). However, Figs 4d and 4e show that proliferating cells are also present in shallow locations. In summary, these findings indicate, for deep inoculation, less localized necrosis and more proliferation than for shallow inoculation.

The smaller number of AuNPs per cell makes the proliferating cells not as easy to observe as dead cells. However, we could track the tumor development by imaging the microvasculature by microangiography. Significantly more microvasculature could be observed in the tumor core for deep inoculation (Figs. 4f–h) than for shallow inoculation (Figs. 3d–h): this could be linked to the faster tumor growth.

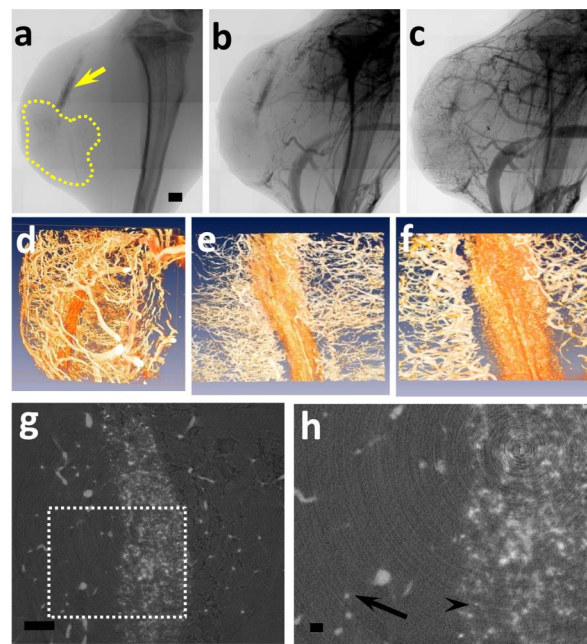


Figure 3 | (a) to (c): x-ray snapshots from a sequence taken after injection of the BaSO_4 nanoparticle colloid contrast agent. The images refer to day 9 after shallow inoculation. (a): before the contrast agent injection, the primary EMT-6 cells (yellow arrow) and the proliferated daughter cells (yellow dotted line) can be observed in two different areas; (b) and (c): with the arrival of the contrast agent, we see the tumor-induced angiogenesis. (d–f) Tomographically reconstructed images corresponding to (c) with increasing magnification (supplementary data S3 d–f). (g): horizontal slice of (f); (h): magnified portion of the same slice. We can see here vessels as narrow as 8 μm (black arrow) and 4 μm wide AuNP aggregates (e.g., the arrow head). The scale bars in (a–c) correspond to 500 μm and those in (g) and (h) to 100 μm and 20 μm .

In addition, tomographically reconstructed images (Figs 4f–h) of the leaky areas (blood pools) also revealed a lymphatic microvasculature network. This might be an interesting point since the possible involvement of the lymphatic vasculature in the tumor development is still not an entirely clarified issue.

The above results were cross-checked with pathologic images (Figs. 5a–5e) showing that the AuNP distribution in the tumor induced by shallow inoculation is consistent with them. High-resolution TXM images (Figs. 5f–5n) further confirmed the distribution of AuNPs: the highest concentration of AuNPs was found at the inoculation site (Figs. 5m and 5n) and decreased at faraway locations (Figs. 5k and 5l). Once again, we saw that parts of the cells were affected by apoptosis at the inoculation site -- see the pathology images of Fig. 5c and 5d and the TXM image of 5m and 5n exhibited a characteristic morphology with shrunk cytoplasm. No angiogenesis microvessels were found at the inoculation site as it is clear in the 3D reconstructed images of Figs. 2g and 2h.

The fast concentration decrease of AuNPs away from the core cannot be explained only by cell migration, whereas it can be justified by proliferation. This is quite evident from TXM images that directly reveal AuNP aggregates; in particular, almost no aggregates are observed away from the core (Fig. 5j).

In addition to tumor development near the inoculation site, we also traced AuNP labeled tumor cells in areas very far from the inoculation site. Specifically, we studied in the metastasis mouse model^{37,38} the lungs after tail vein injection of CT-26 colon cancer cells. The cancer cells were passively transported to the lungs and then developed lung tumors mimicking metastasis. In our tests, we found that initially the cells were attached to vessel walls, and then

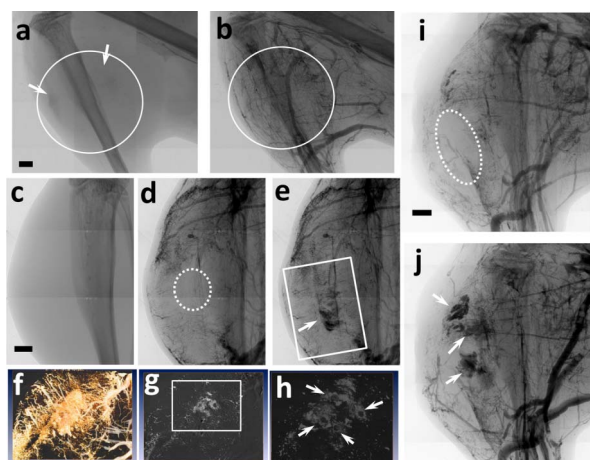


Figure 4 | Images of 3 and 6 day tumors after deep inoculation.

(a) and (b): projection views at day 3 without and with the contrast agent. The arrows within the white circle mark the location of tumor cells (a). The angiogenesis appears much more aggressive than that for shallow inoculation (Fig. 2a). (c)–(e): projection images at day 6 before and after the contrast agent injection showing again strong angiogenesis. Note in (e) (arrow) the blood pools not visible in the empty (dotted) area of (d). (f): tomographically reconstructed image of the rectangular area of (e) (supplementary data S4 f), again revealing that the blood pools coexist with angiogenesis. (g) and (h): tomographic slice of (f) with two different magnifications, showing lymphatic vessels (arrows). (i)–(j): projection images at day 6 similar to (d) and (e), confirming the presence of blood pools. The bars correspond to 1 mm.

started to proliferate. We did not detect any AuNP-loaded cells in other organs, thus confirming that this image strategy can detect such cells far from the inoculation site.

The x-ray microradiology images of Fig. 6 a and b show the related distribution of AuNP aggregates ($>3 \mu\text{m}$) in the lung tissue. The TXM micrographs of Figs. 6 c, d and f were able to detect $<60 \text{ nm}$ nanoparticles in tumor cells and reveal cancer cells near the lung capillary vessels. Such small nanoparticle aggregates are not visible in the pathology optical images (Fig. 6e) whose detection is limited to aggregates larger than 200 nm . Figures 6f and 6g show tomography results: 6f is a projection image part of a tomography set and 6g a reconstructed image, showing cells with AuNPs together with erythrocytes.

We also exploited a new, recently developed type of AuNP³⁶ to extend this tracing approaching to visible light. Using again fast x-ray synthesis but with MUA as capping agent, the nanoparticles were found to become photoluminescent, emitting light at $\sim 602 \text{ nm}$ under 290 nm UV irradiation, when the Au core size was smaller than 1.2 nm . The MUA-AuNPs are highly biocompatible up to a concentration of 1 mM and can produce strong red fluorescence when a sufficient quantity is internalized into cells. We specifically measured by ICP-MS (inductively coupled plasma mass spectrometry), that an average of 57 pg , equivalent to 2.1×10^9 of AuNPs was loaded to each cell during 48 hr of culture with 1 mM of MUA-AuNP. The strong fluorescence is visible in subcutaneous inoculation cases even after 30 days. Supplementary data Fig. S7 shows preliminary results of this approach. Right after the inoculation, Figs. S7 a and S7 b the red fluorescence is very bright and remain visible 7 days after the inoculation (Figs. S7 c and S7 d). At the same time, the x-ray microscopy images of Fig. S7 e and S7 f indicate that the amount of MUA-AuNP loaded into EMT-6 cells is sufficient to affect the transmitted x-ray intensity so that we can locate the cell in the mouse thigh after inoculation as well as with bare AuNPs.

Pathology examination of tissue removed from the tumor shows that the photoluminescence is still present long after the inoculation

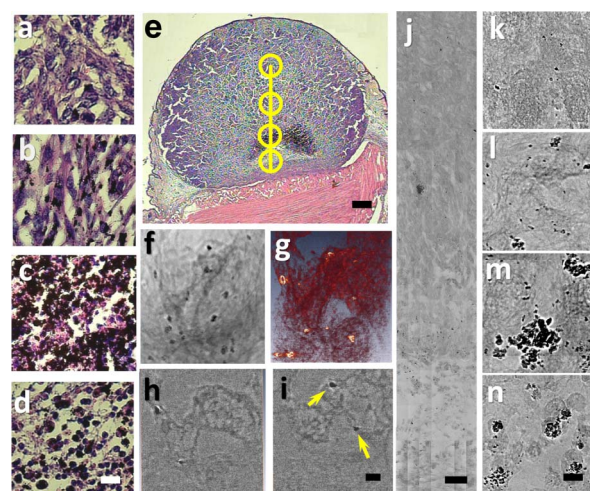


Figure 5 | (a)–(e): Optical pathologic images of a subcutaneous tumor induced by shallow inoculation of AuNPs marked tumor cells.

(a)–(d): magnified views of the areas marked by the circles in (e), ordered from top to bottom (a): Area far from the inoculation site (the darkest area in (e), marked by an arrow, reflects the highest Au concentration); very few AuNPs are detected in the daughter cells. Note that the original inoculated (mother) cells suffer necrotic death with shrunk cytoplasm, particularly those near the muscle tissue (the red part in (e)). The scale bar in (a)–(d): $20 \mu\text{m}$ and (e): $200 \mu\text{m}$. (f)–(n): Nano resolution TXM images. The patched micrographs (j) correspond to the area marked by the line in (e). (k)–(n) refer to the same areas as (a)–(d). (g): tomographically reconstructed image of a daughter cell (red) with AuNP clusters (golden dots) in the rectangular area of (f) (supplementary data S5 g). The scale bars: (k)–(n): $5 \mu\text{m}$ and (j): $50 \mu\text{m}$. (h), (i): tomographically reconstructed image of part of region (f): the bright spots are AuNP aggregates (g).

and therefore allows the identification at the cellular level of the presences of MUA-AuNPs. Those cells loaded with fluorescent MUA-AuNPs can still similarly strong red fluorescence more than 30 days after inoculation to mouse tissues (supplementary data Fig. S7 g) which facilitate a convenient confirmation of the pathological examination as well as visual observation.

Note that the fluorescence in Fig. S7 d is much weaker than in Fig. S7 b since the originally inoculated cells are buried under the thick tumor tissue (as seen in the x-ray image of Figs. S7 e and S7 f) as the tumor grows. Correlated the observed fluorescence in Fig. S7 d and x-ray contrast in Fig. S7 e, we can conclude that those fluorescent red light remaining in the Fig. S7 d are not likely those from the originally inoculated cells buried $>1 \text{ mm}$ under the skin tissue. The fluorescent light still visible in Fig. S7 d, therefore, must be due to daughter cells carrying decreasing amounts of MUA-AuNPs, which is no longer detectable by X-rays, after a few generations of cell divisions, but located at a much shallower position beneath the skin.

Discussion

The successful development of AuNP based contrast agent for X-ray imaging was augmented by a novel approach at cell level imaging. We first confirm that the AuNPs are highly stable and biocompatible by demonstrating that the proliferation rate of the tumor cells loaded with a high concentration of AuNPs did not differ from the value with no nanoparticles. These loaded tumor cells therefore maintain their ability to develop tumor after inoculation into animals. The partition of AuNPs with respect to cell proliferation provides means to estimate the generation in the proliferation from their x-ray contrast. Combined with the development of X-ray based microangiography imaging techniques, whose ability to perform complete profiling of microvasculature of tumor angiogenesis was recently

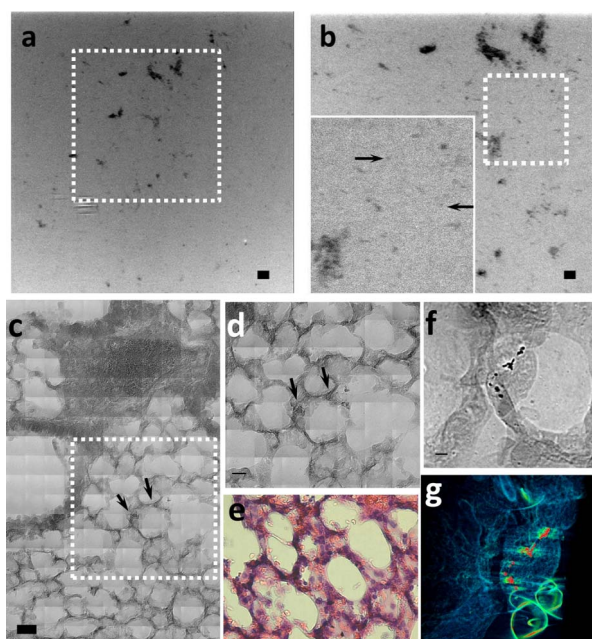


Figure 6 | (a) and (b): projection x-ray images at two magnification levels of unstained lung tissues with AuNPs in formalin solution. The black dots reveal AuNPs in CT-26 cells after injection in the tail. (c) and (d): nanoresolution projection TXM images with two different magnification levels of lung cancer tissues with AuNPs (some marked by arrows) of CT-26 cells. The optical pathologic image in (e) does not show the AuNPs. (f) and (g): tomography results; specifically, (f) is a projection image from a tomography set and (g) the corresponding tomography reconstructed image of the rectangular area of (e) (supplementary data S6 g), revealing <60 nm nanoparticles in tumor cells, seen as black dots in (f) and red dots in (g). The scale bars in (a) and (b) are 50 and 25 μm , in (c)–(d) 24 and 12 μm , and in (f) 1.7 μm .

demonstrated³⁹, this imaging technology offers a reliable imaging method to trace tumor cells, their proliferation and development and, most interestingly, their relation with respect to the tumor angiogenesis in animal models.

Although there were no morphological changes in the animals during in vivo imaging, the current radiation level is quite high and radiation effects on the tumors and their growth cannot be ruled out without more comprehensive tests.

The nanotomography analysis of the locations of the AuNPs in tissues confirmed the role of AuNPs as contrast and tracing agents at sub-cellular level. The discovery of the strong photoluminescent in very small AuNPs and the possibility for additional surface conjugation could promote multimodality imaging with x-ray and visible light microscopy.

With these technical developments, we were able target key questions in the tumor microangiogenesis. Specifically, the main findings are: (1) the AuNP concentrations obtained with our method enabled us to image cancer cells and follow their behavior; (2) such concentrations did not affect the cell capability to proliferate; (3) for shallow inoculation, there was substantial necrosis at the inoculation site, accompanied by proliferation away from it; (4) for deep inoculation, proliferation increased and local necrosis was less relevant; (5) finally, for deep inoculation we also observed migration to large distances from the inoculation site.

Methods

AuNP synthesis and characterisation. Two types of AuNP were used in this study: bare and MUA-coated. The synthesis and characterization procedures were reported previously^{30–36}. In short, these AuNPs are synthesized by a one-pot, reducing-agent-free method taking advantage of the extremely intense x-rays from synchrotron sources. Compared to previous studies exploring AuNPs as contrast agents, our

synthesis method offers reducing agent-free surfaces and excellent size control (because of the fast reaction). These factors positively affect the colloidal stability and biocompatibility and allow high-level loading of AuNPs as required for this imaging strategy.

The specific photoluminescent properties and the cytotoxicity of MUA-AuNPs were characterized previously^{31–32}. The intense red (602 nm) fluorescent emission with UV irradiation is a result of the high quantum efficiency ($>5\%$) and increased the effectiveness of our imaging strategy, allowing tests with UV confocal microscopy.

Cell culture. EMT-6 cells and CT-26 cells were obtained from American Type Culture Collection (ATCC) and cultured at 37°C in humid air with 5% CO₂. EMT-6 cells were incubated with Dulbecco's Modified Eagle's Medium: Nutrient Mixture F-12 (DMEM/F12)/10% fetal calf serum (FCS). CT-26 cells were incubated with RPMI-1640/10% FCS. All media were supplied by Gibco.

Proliferation tests. EMT-6 cells were co-cultured with 500 μM AuNPs^{26–28} for 24 hr, after 1x trypsin treatment. EMT-6 cells with and without AuNPs were separately seeded on a culture dish; the cells were continuously cultured and the cell number was counted every two days. We also compared the cell counting results for cells exposed to AuNPs and unexposed control cells, taking the ratio to assess the effects of the nanoparticles on proliferation.

Tumor development. To load the AuNPs, the EMT-6 cells and CT-26 cells were cultured with 500 μM AuNPs or 500 μM MUA-AuNPs for 24 hr, after 1x trypsin treatment. The amount of Au loaded per cell was measured by ICP-MS, obtaining 20 pg for bare AuNP and 28 pg for MUA-AuNP. Then, harvested cells were added to PBS. 50 μl of 1×10^7 cells/ml EMT-6 cell solution were inoculated in the subcutaneous tissue of the left leg region using a 29 gauge needle and an injection rate of 10 $\mu\text{L}/\text{sec}$. To investigate the effect of the inoculation site to tumor growth, two different sites were tested. For shallow inoculation, the needle was inserted into the subcutaneous tissue nearly parallel to the skin. Insertion at an angle ~ 15 degree with respect to the skin surface resulted in an inoculation point ~ 1 mm below the skin surface, with the needle partially entering the thigh muscle region. For the lung tumor metastasis model, 100 μl 1×10^7 cells/ml of the CT-26 cell solution, were introduced by tail vein injection at an injection rate of 10 $\mu\text{L}/\text{s}$ with a 29 gauge needle.

All procedures involving animals were approved by the Academia Sinica Institutional Animal Care and Utilization Committee (AS IACUC). BALB/cByJNarl mice were provided by National Laboratory Animal Center, Taiwan. All mice were housed in individual ventilated cages (five per cage) with wood chip bedding and kept at $24 \pm 2^\circ\text{C}$ with a humidity of 40%–70% and a 12-hour light/dark cycle. The subcutaneous tumor volume was estimated with the formula $v = 0.5 \times a \times b^2$, where a and b are the smallest and the largest diameters. Tumor imaging started after ≈ 7 days, when they reached a size of 100 to 120 mm^3 . Overall, 18 mice were used in this experiment; 7 were shallow-inoculated with AuNP loaded cells and 3 were deep-inoculated. Control experiment in which the injected cells were without AuNP concerned 10 mice, 6 for shallow and 4 for deep inoculation. The results were statistically analyzed with the ANOVA by GraphPad Prism 4 software.

In vivo x-ray imaging. Microradiology was implemented with unmonochromatized (white) synchrotron x-rays emitted by the 01-A beamline wavelength shifter of the National Synchrotron Radiation Research Center (Taiwan)^{40–42}. The photon energy ranged from 4 keV to 30 keV with a peak intensity at energy ~ 12 keV and the beam current was kept constant at 360 mA with the top-up operation mode. To obtain 4.5×3.4 mm images, the x-rays were first converted to visible light by a CdWO₄ single crystal scintillator and then captured by an optical microscope with a CCD camera (model 211, Diagnostic instruments, 1600×1200 pixel). The radiation dose was reduced by attenuating the emitted x-ray beam with two pieces of 550 μm single crystalline silicon wafers placed before the animal. During x-ray imaging, the mice were kept under anesthesia using 1% isoflurane in oxygen. Tissues and organs were removed from sacrificed animal right after microradiology tests for tomography and additional TXM imaging.

The exposure time was ~ 100 ms with a dose of ~ 34 Gy and the distance between the sample and the scintillator was ≈ 5 cm; a 2x lens in the optical microscope was used to obtain the desired field of view. The size of each pixel in the final image taken with the 2x lens was $\approx 2.8 \times 2.8$ μm^2 . To follow the circulation dynamics of the contrast agents, 5–10 images were recorded with further attenuation of the x-rays to keep the accumulated dosage below 100 Gy.

Tissue sample preparation. After developing subcutaneous or lung tumors, the mice were sacrificed by an overdose of Zoletil 50 (50 mg/kg; Virbac Laboratories, Carros, France) administered by intramuscular injection (weight ~ 20 –25 g); then, subcutaneous tissues and lungs were removed. Tissue specimens were immersed in the 3.7% paraformaldehyde for 24 hr. After fixation, the tissues were washed by PBS (phosphate buffer solution) three times for 1 hr. Before embedding, the tissues were separated in two groups for x-ray imaging with micro resolution and nano resolution.

Micro resolution x-ray tomography imaging was performed on thick tissue specimens embedded in resin. Nano resolution x-ray imaging was performed instead with specimen embedded in paraffin. All tissues were dehydrated by subsequent immersions in ethanol solutions, from low to high concentration, and then embedded in the resin or paraffin. The specimens for nano resolution were sliced to ≈ 30 μm thickness and immersed in Xylene for three times per 5 minutes to remove the remaining wax. Then, the specimens were dehydrated with the same procedure



described above and immersed in distilled water. The specimens were then processed with heavy metal staining (osmium), washed with distilled water 3 times for 5 minutes, dehydrated as above and embedded in Embed-812 Resin (EMS, Hatfield, PA). The same procedure as for x-ray nanoimaging was followed to prepare specimens for optical microscopy except that the heavy metal staining was replaced by H&E staining.

Tomography. Thick samples in resin were used to take sets of 1000 images at equal angular distance within 180 degrees; tomographic reconstruction was then performed with the IDL software. All reconstructed images were processed with the Amira 5.2 software to obtain three dimensional pictures.

High resolution x-ray imaging. These tests were performed on the 32-ID microscopy beamline of the Advanced Photon Source (APS) at the Argonne National Laboratory. Our full-field x-ray transmission microscope (TXM) uses a set of capillary condensers to precisely illuminate the object by a numerical aperture matched to the Fresnel zone plate (FZP) objectives. The condensers are elliptically shaped glass capillaries. The inner diameter of 0.9 mm was chosen to maximize the vertical acceptance of the APS undulator beam at 65 m from the source.

The estimated monochromatic x-ray flux through a Si (111) double crystal monochromator focused by the condenser was 2×10^{11} photons/s at 8 keV. The high brightness of the APS and the optimized condensers design yielded an excellent imaging rate of 50 ms/frame with $\sim 1 \times 10^4$ CCD (charge coupled device) counts per pixel. We used for all images phase contrast with a Au Zernike phase ring placed at the back focal plane of the FZP objective^{5,6}.

- Chien, C. C. *et al.* Synchrotron microangiography studies of angiogenesis in mice with microemulsions and gold nanoparticles. *Anal Bioanal Chem* **397**, 2109–2116 (2010).
- Cai, Q. Y. *et al.* Colloidal gold nanoparticles as a blood-pool contrast agent for X-ray computed tomography in mice. *Invest Radiol* **42**, 797–806 (2007).
- Hainfeld, J. Gold nanoparticles: a new X-ray contrast agent. *The British Journal of Radiology* **79**, 248–253 (2006).
- Menk, R. H. *et al.* Gold nanoparticle labeling of cells is a sensitive method to investigate cell distribution and migration in animal models of human disease. *Nanomedicine: Nanotechnology, Biology and Medicine* **7**, 647–654 (2011).
- Reuveni, T. *et al.* Targeted gold nanoparticles enable molecular CT imaging of cancer: an in vivo study. *International Journal of Nanomedicine* **6**, 2859–2864 (2011).
- Chen, H. *et al.* Optical imaging in tissue with X-ray excited luminescent sensors. *Analyst* **83**, 5045–5049 (2011).
- Lewis, D. J. *et al.* Intracellular synchrotron nanoimaging and DNA damage/genotoxicity screening of novel lanthanide-coated nanovectors. *Nanomedicine* **5**, 1547–1557 (2010).
- Jiang, W., Papa, E., Fischer, H., Mardiyani, S. & Chan, W. C. Semiconductor quantum dots as contrast agents for whole animal imaging. *Trends Biotechnol* **22**, 607–609 (2004).
- Jaiswal, J. K. & Simon, S. M. Potentials and pitfalls of fluorescent quantum dots for biological imaging. *Trends Cell Biol* **14**, 497–504 (2004).
- Chen, Y. T. *et al.* Full-field hard x-ray microscopy below 30 nm: a challenging nanofabrication achievement. *Nanotechnology* **19**, 395302 (2008).
- Chen, Y. T. *et al.* Full-field microimaging with 8 keV X-rays achieves a spatial resolutions better than 20 nm. *Optics Express* **19**, 19919–19924 (2011).
- Jain, R. K. & Stylianopoulos, T. Delivering nanomedicine to solid tumors. *Nat Rev Clin Oncol* **7**, 653–664 (2010).
- Brannon-Peppas, L. & Blanchette, J. O. Nanoparticle and targeted systems for cancer therapy. *Adv Drug Deliv Rev* **56**, 1649–1659 (2004).
- Yokoyama, M. Drug targeting with nano-sized carrier systems. *J Artif Organs* **8**, 77–84 (2005).
- Prabakaran, M., Grailer, J. J., Pilla, S., Steeber, D. A. & Gong, S. Gold nanoparticles with a monolayer of doxorubicin-conjugated amphiphilic block copolymer for tumor-targeted drug delivery. *Biomaterials* **30**, 6065–6075 (2009).
- Li, J. *et al.* The enhancement effect of gold nanoparticles in drug delivery and as biomarkers of drug-resistant cancer cells. *ChemMedChem* **2**, 374–378 (2007).
- Popovtzer, R. *et al.* Targeted Gold Nanoparticles Enable Molecular CT Imaging of Cancer. *Nano Letters* **8**, 4593–4596 (2008).
- Arvizo, R. R. *et al.* Mechanism of anti-angiogenic property of gold nanoparticles: role of nanoparticle size and surface charge. *Nanomedicine: Nanotechnology, Biology and Medicine*, doi:10.1016/j.nano.2011.01.011.
- Lee, S. Y. *et al.* In situ single cell monitoring by isocyanide-functionalized Ag and Au nanoprobe-based Raman spectroscopy. *J Microbiol Biotechnol* **19**, 904–910 (2009).
- Sharma, P. *et al.* Multimodal nanoparticulate bioimaging contrast agents. *Methods Mol Biol* **624**, 67–81 (2010).
- Hahn, M. A., Singh, A. K., Sharma, P., Brown, S. C. & Moudgil, B. M. Nanoparticles as contrast agents for in-vivo bioimaging: current status and future perspectives. *Anal Bioanal Chem* **399**, 24 (2010).
- Boote, E. *et al.* Gold nanoparticle contrast in a phantom and juvenile swine: models for molecular imaging of human organs using x-ray computed tomography. *Acad Radiol* **17**, 410–417 (2010).
- Patel, P. C. *et al.* Scavenger Receptors Mediate Cellular Uptake of Polyvalent Oligonucleotide-Functionalized Gold Nanoparticles. *Bioconjug Chem* **21**, 2250–2256 (2010).

- Li, G., Li, D., Zhang, L., Zhai, J. & Wang, E. One-step synthesis of folic acid protected gold nanoparticles and their receptor-mediated intracellular uptake. *Chemistry* **15**, 9868–9873 (2009).
- Hall, C. J. *et al.* Synchrotron-based in vivo tracking of implanted mammalian cells. *Eur J Radiol* **68**, S156–S159 (2008).
- Zhang, Q., Hitchins, V. M., Schrand, A. M., Hussain, S. M. & Goering, P. L. Uptake of gold nanoparticles in murine macrophage cells without cytotoxicity or production of pro-inflammatory mediators. *Nanotoxicology* **5**, 284–295 (2011).
- Taylor, U. *et al.* Nonendosomal cellular uptake of ligand-free, positively charged gold nanoparticles. *Cytometry A* **77**, 439–446 (2010).
- Sadauskas, E. *et al.* Kupffer cells are central in the removal of nanoparticles from the organism. *Part Fibre Toxicol* **4**, 10 (2007).
- Balogh, L. *et al.* Significant effect of size on the in vivo biodistribution of gold composite nanodevices in mouse tumor models. *Nanomedicine* **3**, 281–296 (2007).
- Chen, H. H. *et al.* Quantitative analysis of nanoparticle internalization in mammalian cells by high resolution X-ray microscopy. *J Nanobiotechnology* **9**, 14 (2011).
- Lai, S. F. *et al.* Size control of gold nanoparticles by intense X-ray irradiation: the relevant parameters and imaging applications. *RSC Adv*, DOI:10.1039/C2RA20260C.
- Lai, S. F. *et al.* Very Small Photoluminescent Gold Nanoparticles for Multimodality Biomedical Imaging. *J. Biotech. Adv.* 10.1016/j.jbiotechadv.2012.05.005.
- Wang, C. H. *et al.* Aqueous gold nanosols stabilized by electrostatic protection generated by X-ray irradiation assisted radical reduction. *Materials Chemistry and Physics* **106**, 323–329 (2007).
- Yang, Y. C., Wang, C. H., Hwu, Y. K. & Je, J. H. Synchrotron X-ray synthesis of colloidal gold particles for drug delivery. *Mater Chem Phys* **100**, 72–76 (2006).
- Wang, C. H. *et al.* Structural properties of ‘naked’ gold nanoparticles formed by synchrotron X-ray irradiation. *J Synchrotron Radiat* **14**, 477–482 (2007).
- Lai, S. F. *et al.* One-pot Tuning of Au Nucleation and Growth: From Nanoclusters to Nanoparticles. *Langmuir* **27**, 8424–8429 (2011).
- Brattain, M. G., Strobel-Stevens, J. Fine, D., Webb, M. & Sarraf, A. M. Establishment of Mouse Colonic Carcinoma Cell Lines with Different Metastatic Properties. *Cancer Research* **40**, 2142–2146 (1980).
- Zeelenberg, I. S., Ruuls-Van Stalle, L. & Roos, E. The Chemokine Receptor CXCR4 Is Required for Outgrowth of Colon Carcinoma Micrometastases. *Cancer Research* **63**, 3833–3839 (2003).
- Chia-Chi, Chien *et al.* Complete microscale profiling of tumor microangiogenesis: A microradiological methodology reveals fundamental aspects of tumor angiogenesis and yields an array of quantitative parameters for its characterization. *Biotechnology Advances*. doi:10.1016/j.biotechadv.2011.12.001 (2012).
- Hwu, Y., Je, J. H. & Margaritondo, G. Real-time radiology in the microscale. *Nuclear Instruments & Methods in Physics Research Section a-Accelerators Spectrometers Detectors and Associated Equipment* **551**, 108–118 (2005).
- Hwu, Y. *et al.* Synchrotron microangiography with no contrast agent. *Physics in Medicine and Biology* **49**, 501–508 (2004).
- Hwu, Y. *et al.* Coherence-enhanced synchrotron radiology: Refraction versus diffraction mechanisms. *Journal of Applied Physics* **86**, 4613–4618 (1999).

Acknowledgements

Work supported by the ANR-NSC French-Taiwan bilateral program n° ANR-09-BLAN-0385, the National Science and Technology Program for Nanoscience and Nanotechnology, the Thematic Research Project of Academia Sinica, the Biomedical Nano-Imaging Core Facility at National Synchrotron Radiation Research Center (Taiwan), the Fonds National Suisse pour la Recherche Scientifique and the CIBM. Imaging work performed at Advanced Photon Source is supported by the U. S. Department of Energy, Office of Sciences, Office of Basic Energy Sciences, under Contract No. DE-AC02-06CH11357.

Author contributions

CCC designed and performed experiments, analysed data and wrote the paper; HHC, YC and SFL performed experiments; YC, CP, CSY developed analytical tools and analysed data; YH and GM designed experiments, developed analytical tools, analysed data and wrote the paper.

Additional information

Supplementary information accompanies this paper at <http://www.nature.com/scientificreports>

Competing financial interests: The authors declare no competing financial interests.

License: This work is licensed under a Creative Commons Attribution-NonCommercial-NoDerivative 3.0 Unported License. To view a copy of this license, visit <http://creativecommons.org/licenses/by-nc-nd/3.0/>

How to cite this article: Chien, C. *et al.* X-ray imaging of tumor growth in live mice by detecting gold-nanoparticle-loaded cells. *Sci. Rep.* **2**, 610; DOI:10.1038/srep00610 (2012).